scientific reports

Check for updates

OPEN

# Investigating the potential of triclinic $ABSe_3$ (A = Li, Na, K, Rb, Cs; B = Si, Ge, Sn) perovskites as a new class of lead-free photovoltaic materials

Eman Khalafalla Mahmoud, S. I. El-dek, Ahmed A. Farghali & Mohamed Taha ✉

**In recent years, chalcogenide perovskites have emerged as promising candidates with favorable structural, electrical, and optical properties for photovoltaic applications. This paper explores the structural, electronic, and optical characteristics of $ABSe_3$ perovskites (where A = Li, Na, K, Rb, Cs; B = Si, Ge, Sn) in their triclinic crystallographic phases using density functional theory. The stability of these materials is ensured by calculating formation energies, tolerance factors ($T_f$), and phonon dispersion. The $E_{form}$ values of all $ABSe_3$ are negative, suggesting favorable thermodynamic stability. The $T_f$ values range between 0.82 and 1.1, which is consistent with stable perovskites. The phonon dispersion analysis of the chalcogenide perovskites revealed no imaginary frequencies in any of the vibrational modes, confirming their stability. The electronic band structures and corresponding density of states are computed to unveil the semiconducting nature of the studied compounds. These perovskites are promising for high-performance solar cells due to their indirect bandgaps ($E_g$, 1.10–2.33 eV) and a small difference between these indirect and direct gaps (0.149–0.493 eV). The $E_g$ values increase as the ionic radii of A-site elements increase (Li < Na < K < Rb < Cs). At the B-site, Si-based chalcogenides have the largest $E_g$ values, followed by Sn-based and then Ge-based materials. Furthermore, optical properties such as the real part and imaginary part of the dielectric function, refractive index extinction coefficient, optical conductivity, absorption coefficient, reflectivity, and energy loss are predicted within the energy range of 0–50 eV. Several $ABSe_3$ materials, particularly $LiGeSe_3$ and $NaGeSe_3$, demonstrated optical properties comparable to both traditional and emerging materials, suggesting their potential for effective use in solar cells.**

**Keywords** Chalcogenide perovskites, Density functional theory, Electronic properties, Optical properties, Solar cell applications

Due to the increasing global energy use, and as currently available energy sources are mostly based on fossil fuels, researchers are increasingly focused on developing renewable energy resources[1,2]. Solar energy, a vital source of renewable energy, can be harnessed through thermoelectric and photovoltaic technologies. These technologies convert heat and light from the sun into electrical energy[3]. The selection of materials is crucial for determining their suitability in thermal applications (e.g., thermoelectric devices) and photoelectric applications (e.g., solar cells) due to their property dependence (conductivity, band gap)[4].

Perovskite materials may play a crucial role in this regard because of their extraordinary physical properties such as magnetic, ferroelectric, optical, charge ordering, spin-dependent transport and high thermoelectric power[5,6]. Within the diverse perovskite family (oxide, halide, and chalcogenide)[7–13], chalcogenide perovskites, with a general formula $ABX_3$ (where A and B represent cations of different sizes and X is a chalcogenide element S, Se, or Te), are attracting attention for their potential in solar energy conversion due to their favorable structural, optical, and electronic characteristics. Oxide and halide perovskites have long been exhibiting remarkable properties for solar energy conversion[14–16]. For instance, various perovskite materials displayed promise in several technological applications. Compounds like $A_2NiMnO_6$ (A = La, Gd)[17], $Ca_2NaIO_6$[18], $Sr_2NaIO_6$[18], $RbPbBr_3$[19], $RbPbI_3$[19],

Materials Science and Nanotechnology Department, Faculty of Postgraduate Studies for Advanced Sciences (PSAS), Beni-Suef University (BSU), Beni-Suef, Egypt. ✉email: mtaha@psas.bsu.edu.eg

and $Rb_2NaCoX_6$ (X = Cl, Br, I)[20] exhibit properties suitable for magneto-caloric refrigeration, photocatalysis, thermoelectric energy conversion, and other applications due to their favorable structural, electrical, optical, and transport characteristics. However, oxide perovskites often exhibit limitations for solar energy conversion due to their wide band gaps[21]. This limitation arises from the high electronegativity of oxygen, which typically results in bandgaps positioned in the ultraviolet (UV) region. On the other hand, halide perovskites suffer from toxicity, moisture, and thermal instability[22].

Lead-based perovskites have attracted considerable interest for their outstanding optoelectronic properties, particularly in solar cell applications. However, the toxicity of lead raises significant environmental and health concerns, prompting researchers to explore lead-free alternatives[5,11]. The development of environmentally friendly lead-free perovskites solar cells has become crucial to realize their large-scale production. To address this challenge, several novel lead-free perovskite materials have been explored both computationally and experimentally[23–26]. A computational study using density functional theory (DFT) of ethylammonium tin chloride ($C_2H_5NH_3SnCl_3$) has shown that this material can exhibit favorable electronic band structure and optical properties, making it suitable for thermoelectric applications[27]. Recent computational studies, such as that by Riku et al.[28], have identified lead-free $ABX_3$ (A = Rb or Cs, B = Sn, Sr, or Ca, X = Cl, Br, or I) perovskites are ideal for solar cells and light-emitting diodes[28]. Sarker et al. demonstrate that $NaGeX_3$ (X = F, Cl, Br, and I) is beneficial and non-toxic for solar cell applications[29]. DFT computation of $KSnI_3$, $KSn_{0.5}Ge_{0.5}I_3$, and $KGeI_3$ demonstrate their capability as a functional layer in nontoxic perovskite solar cells[30].

Chalcogenide perovskites offer superior environmental stability compared to halide perovskites, making them ideal for long-term applications like solar cells, where exposure to moisture and heat can degrade performance[31]. They are also composed of non-toxic elements, making them more environmentally friendly and safer for commercial use[1,7,31]. Chalcogenide perovskites can achieve high absorption coefficients, which enhances their efficiency as photoabsorbers[32]. Their covalent nature improves electronic and optical performance, leading to better charge transport and reduced recombination losses[33]. Additionally, they possess higher thermal and moisture stability than oxide perovskites, crucial for maintaining device performance[31]. Finally, chalcogenide perovskites offer tunable bandgap structures, optimizing their performance for applications like tandem solar cells[23,33].

Recently, a diverse range of chalcogenide perovskites with interesting properties has been both experimentally verified and theoretically predicted[31,34–39]. Perera et al.[40] reported the successful synthesis of several chalcogenide perovskites, including $BaZrS_3$, $CaZrS_3$, $SrZrS_3$, and $SrTiS_3$. These materials exhibit unique physical properties, such as being free of deep-level defects, which is beneficial for energy harvesting and other optoelectronic applications. Shaili et al. reported that synthesized $CaSnS_3$ exhibits a suitable bandgap of 1.72 eV for optoelectronic applications[41]. $SrZrS_3$ and $SrZrSe_3$ may be employed as a photovoltaic absorber coating inside solar cells, as well as in energy conversion devices owing to their acceptable optical and thermoelectric properties[42]. Naincy et al. predicted the applicability of $BaZrS_3$ and $BaZrSe_3$ in energy conversion device fabrication[43]. Nishigaki et al. reported the synthesis of $BaZrS_3$, $SrZrS_3$, $BaHfS_3$, and $SrHfS_3$, distorted chalcogenide perovskites, with a direct bandgap (1.94–2.41 eV), making them suitable solar cell light absorbers[44]. Furthermore, Majhi synthesized $FeNiSe_2$ and FeNiSSe as efficient electrocatalysts for water splitting[45].

DFT studies have yielded promising chalcogenide perovskite candidates for solar cells. Sun et al.[46] identified $CaTiS_3$, $BaZrS_3$, $CaZrSe_3$, and $CaHfSe_3$ as promising candidates for single-junction solar cells. Similarly, Du et al.[47,48] proposed $Ca_3Sn_2S_3$ and $ACeTe_3$ (A = Ca, Sr, Ba) as suitable photovoltaic materials. Likewise, Thakur et al.[49] and Liu et al.[50] predicted the potential of $ABX_3$ (A = Ba, B = Zr, X = S and/or Se) and $ABSe_3$ (A = Ca, Sr, Ba; B = Hf, Zr) for photovoltaic applications, respectively. Zhang et al.[51] further extended this investigation to $LaScSe_3$ for optoelectronic applications. Earlier research has highlighted the potential of chalcogenide perovskites, $ABX_3$ (A = Ca, Sr, or Ba; B = Ti, Zr, or Hf; and X = O, S, or Se) to address the limitations of halide perovskites, particularly regarding concerns about toxicity and stability[52].

In this paper, we employ DFT to predict the structural, electronic, and optical properties of chalcogenide perovskites $ABSe_3$ (A = Li, Na, K, Rb, Cs; and B = Si, Ge, Sn) in triclinic crystallographic phases. The motivation for this study stems from the growing interest in chalcogenide perovskites due to their potential applications in optoelectronics and photovoltaics. Due to the absence of experimental data for comparison with theoretical results on the investigated perovskites, we employed the Heyd-Scuseria-Ernzerhof hybrid functional (HSE06)[53]. It is a hybrid density functional that combines the strengths of Hartree–Fock theory with DFT. It is particularly designed to address some of the limitations associated with local density approximations (LDA) and generalized gradient approximations (GGA), which often underestimate band gaps in semiconductors and insulators. HSE06 is a powerful tool in computational materials science, providing improved accuracy for electronic structure calculations while also presenting some limitations related to computational cost. HSE06 has been shown to accurately predict bandgaps, electrical, and optical properties for a variety of perovskite materials[54].

## Computational method

All calculations were carried out with the CASTEP code[55] within the Materials Studio 2020 package, employing DFT. $CsSnS_3$ (triclinic, P-1,2) was taken from the material project website (mp-561710)[56]. Cs atom was systematically replaced with Li, Na, K, and Rb, while Sn atom was substituted with Si and Ge atoms, and the S atoms were replaced with Se atoms. Geometry optimization, electronic, and optical properties, were conducted using HSE06 hybrid functional[53]. Each exchange–correlation (XC) functional has been calculated using kinetic energy cut-offs of 650 eV with norm-conserving pseudopotential[57]. The self-consistent field (SCF) tolerance was $1.0 \times 10^{-6}$ (eV/atom). Furthermore, the total energy tolerance, maximum ionic Hellmann–Feynman force, and maximum ionic displacement tolerance were $1.0 \times 10^{-5}$ (eV/atom), 0.03 (eV/Å) and 0.001 (Å), respectively. A dense 12 × 12 × 12 Monkhorst and Pack mesh grid was used for k-points sampling of the first Brillouin zone. The phonon dispersion curves for the chalcogenide perovskites were calculated using the GGA/PBEsol method[58].

The optical properties were calculated using HSE functional by the complex dielectric function $\varepsilon(\omega)$ given as[59],

$$\varepsilon(\omega) = \varepsilon_1(\omega) + i\varepsilon_2(\omega), \tag{1}$$

where $\varepsilon_1(\omega)$ and $\varepsilon_2(\omega)$ represents the real and imaginary part of the dielectric constant. The well-known Kramer–Kronig relation connects the real and imaginary sections of the dielectric functions as follows[60,61]:

$$\varepsilon_1(\omega) = 1 + \frac{2}{\pi} P \int_0^{\infty} \frac{\omega' \varepsilon_2(\omega)}{\omega'^2 - \omega^2} \mathrm{d}\omega, \tag{2}$$

where $P$ denotes the principal value of the integral.

$$\varepsilon_2(\omega) = \frac{2e^2\pi}{\Omega\varepsilon_0} \sum_{k,v,c} \left|\psi_k^c\right| u.r \left|\psi_k^v\right|^2 \delta\left(E_k^c + E_k^v - \mathrm{E}\right). \tag{3}$$

Here, u and e represent the polarization of the incident electric field and the electric charge, respectively. Ω denotes the volume of a unit cell. $\psi_k^c$ and $\psi_k^v$ signify the wave functions of the valence band and conduction band, respectively, at the position $k$. By using $\varepsilon_1(\omega)$ and $\varepsilon_2(\omega)$, optical properties like reflectivity $R(\omega)$, absorption coefficient $\alpha(\omega)$, optical conductivity $\sigma(\omega)$, refractive index $n(\omega)$, extinction coefficient $k(\omega)$ and energy-loss spectrum $L(\omega)$ are evaluated as follows[62–64]:

$$R(\omega) = \left| \frac{\sqrt{\varepsilon(\omega)} - 1}{\sqrt{\varepsilon(\omega)} + 1} \right|^2, \tag{4}$$

$$\alpha(\omega) = \frac{\omega}{c} \sqrt{2\left(\sqrt{\varepsilon_1^2(\omega) + \varepsilon_2^2(\omega)} - \varepsilon_1(\omega)\right)}, \tag{5}$$

$$\sigma(\omega) = \frac{i\omega}{4\pi} \varepsilon(\omega), \tag{6}$$

$$n(\omega) = \sqrt{2\frac{\sqrt{\varepsilon_1^2(\omega) + \varepsilon_2^2(\omega)} + \varepsilon_1(\omega)}{2}}, \tag{7}$$

$$k(\omega) = \sqrt{2\frac{\sqrt{\varepsilon_1^2(\omega) + \varepsilon_2^2(\omega)} - \varepsilon_1(\omega)}{2}}, \tag{8}$$

$$L(\omega) = \frac{\varepsilon_2(\omega)}{\varepsilon_1(\omega) + \varepsilon_2(\omega)}. \tag{9}$$

## Results and discussion

### Structural properties

Figure 1 represents the triclinic crystal structure of the chalcogenide perovskite series $ABSe_3$ (A = Li, Na, K, Rb, Cs; B = Si, Ge, Sn). The A-site cation exhibits a larger ionic radius compared to the B-site cation, consistent with the typical structural features of perovskites. For systematic analysis, the investigated chalcogenide perovskites were categorized into three groups based on the B-site cation: Si-based ($ASiSe_3$), Ge-based ($AGeSe_3$), and Sn-based ($ASnSe_3$).

The substitutions at the A, B and X sites can cause significant improvements in stability and performance[65,66]. However, by substitutions, the crystal structure of a perovskite material can alter significantly, which can be anticipated using the Goldschmidt tolerance factor ($T_f$)[67]. The $T_f$, Eq. (8), anticipates the viability of a combination of A, B, and X elements to form a perovskite phase by calculating a structural ratio; a value between 0.80 and 1.11 indicates ideal cubic structures or a distorted perovskite structure with tilted octahedral. Structures having $T_f$ values outside the range cannot be considered stable perovskites[68–70].

$$T_f = \frac{R_A + R_{Se}}{\sqrt{2}(R_B + R_{Se})}. \tag{10}$$

$R_A$, $R_B$, and $R_{Se}$ symbolize the Shannon ionic radii of A, B, and Se elements, respectively[71]. Our investigated perovskites have tolerance factor values ranging from 0.8158 to 1.117 (Table 1), revealing structural stability.

Formation energy ($E_{form}$), which represents the energy required to form a material from its constituent elements, was utilized to assess the thermodynamic stability of the perovskites by Eq. (11)[72],

$$E_{form} = E_{\mathrm{ABSe_3}} - (E_{\mathrm{A}} + E_{\mathrm{B}} + 3E_{\mathrm{Se}})_{\mathrm{atom}}. \tag{11}$$

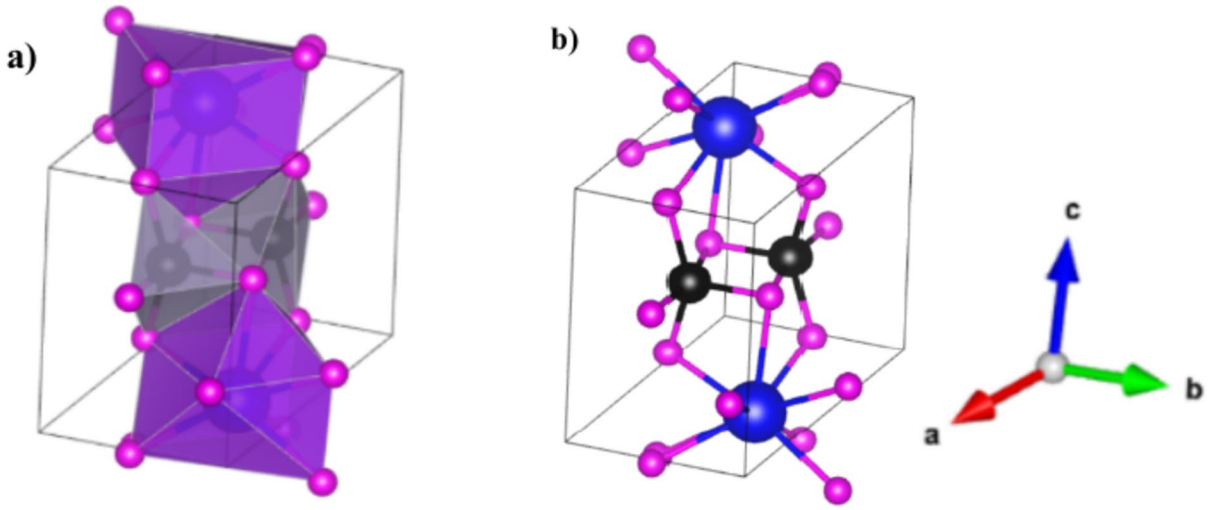


**Fig. 1.** Polyhedral model (**a**) and ball and stick model (**b**) of $ABSe_3$. Blue, black and purple are associated with A, B, and Se atoms.

| Perovskite | $T_f$ | $E_{form}$ | Perovskite | $T_f$ | $E_{form}$ | Perovskite | $T_f$ | $E_{form}$ |
|---|---|---|---|---|---|---|---|---|
| $LiSiSe_3$ | 0.9153 | − 3.84 | $LiGeSe_3$ | 0.8700 | − 3.30 | $LiSnSe_3$ | 0.8158 | − 4.17 |
| $NaSiSe_3$ | 0.9717 | − 4.54 | $NaGeSe_3$ | 0.9213 | − 3.99 | $NaSnSe_3$ | 0.8662 | − 4.70 |
| $KSiSe_3$ | 1.0490 | − 5.10 | $KGeSe_3$ | 0.9946 | − 4.49 | $KSnSe_3$ | 0.8874 | − 5.17 |
| $RbSiSe_3$ | 1.0728 | − 5.11 | $RbGeSe_3$ | 1.0226 | − 4.56 | $RbSnSe_3$ | 0.9562 | − 5.29 |
| $CsSiSe_3$ | 1.117 | − 5.27 | $CsGeSe_3$ | 1.0621 | − 4.70 | $CsSnSe_3$ | 0.9960 | − 5.49 |

**Table 1.** Goldschmidt's tolerance factor ($T_f$) and formation energy ($E_{form}$) for Si-based, Ge-based, and Sn-based chalcogenides using the HSE06 method.

The energies of A, B, and Se atoms in their corresponding bulk crystal phases are denoted by $E_A$, $E_B$ and $E_{Se}$, respectively. $E_{ABSe_3}$ is the energy of the $ABSe_3$ unit cell. Materials having low (negative) formation energies are more stable and less prone to break down into their constituent elements. This stability is essential for sustaining the efficiency of perovskite solar cells over time, particularly in conditions of operation[73]. This stability is critical for assuring the longevity and reliability of perovskite solar cells, which are frequently subjected to changing environmental conditions. The formation energy also influences the development of tandem solar cells, which combine perovskites with silicon or other materials. Perovskite/silicon tandem cells, for example, have achieved efficiencies of more than 31%, demonstrating the potential for optimizing formation energies in multi-junction configurations[74]. For all studied $ABSe_3$, $E_{form}$ was calculated to be negative (Table 1), suggesting favorable thermodynamic stability. Interestingly, within each series (Si, Ge, or Sn), the formation energies exhibit a trend of becoming more negative (increasingly stable) as the A-site cation follows (Li < Cs < Rb < K < Na). Within each A-site cation, the formation energy tends to become more negative as the B-site cation changes from Sn to Ge to Si.

Lattice parameters, unit cell volume (V), and theoretical density (D) were calculated and presented in Table 2. The increasing trend in unit cell volume coincides with an increase in lattice parameters, as a result of the increase in the ionic radius of the A-site cation.

## Phonon dispersion

The calculation of phonon dispersion curves provides valuable insights into the dynamical stability of materials by revealing the vibrational frequencies of atoms within the crystal lattice. The phonon dispersion of a material significantly influences its mechanical properties, such as elasticity and hardness, as well as its thermal behavior, including thermal conductivity and specific heat capacity. These factors collectively determine its overall suitability for practical applications, such as structural components and electronic devices[75,76]. The presence of imaginary frequencies in phonon dispersion curves indicates dynamic instability of the material, whereas their absence signifies stability. Figure 2 depicts the calculated phonon dispersion curves for the chalcogenide perovskites, revealing the absence of imaginary frequencies across all vibrational modes, indicative of their stability[77]. One remarkable feature from Fig. 2 is the band gap in the phonon spectrum. We can see that this band gap was noticed for $NaSiSe_3$, $NaGeSe_3$, $KSiSe_3$, $KGeSe_3$, $RbSiSe_3$, $RbGeSe_3$, $CsSiSe_3$ and $CsGeSe_3$ meanwhile extremely small for other perovskites. The presence of phonon band gaps, regions in the dispersion where no phonon modes exist, can lead to a reduction in thermal conductivity due to the limited number of available heat-carrying channels[77].

| Perovskite | Lattice parameters | | | | | | V (Å$^3$) | D (g/cm$^3$) |
|---|---|---|---|---|---|---|---|---|
| | A (Å) | B (Å) | c(Å) | α° | β° | γ° | | |
| $LiSiSe_3$ | 5.926 | 5.264 | 7.838 | 101.226 | 112.367 | 113.288 | 189.829 | 4.757 |
| $NaSiSe_3$ | 6.544 | 5.600 | 7.323 | 93.536 | 114.181 | 119.514 | 201.029 | 4.757 |
| $KSiSe_3$ | 6.248 | 5.918 | 7.294 | 9.9151 | 15.799 | 8.940 | 226.625 | 4.455 |
| $RbSiSe_3$ | 6.334 | 6.191 | 7.224 | 89.567 | 115.697 | 107.709 | 240.692 | 4.835 |
| $CsSiSe_3$ | 6.706 | 7.182 | 7.586 | 97.726 | 114.212 | 106.905 | 305.078 | 4.331 |
| $LiGeSe_3$ | 6.061 | 5.306 | 8.060 | 100.741 | 113.470 | 14.350 | 196.654 | 5.343 |
| $NaGeSe_3$ | 6.627 | 5.634 | 7.449 | 93.271 | 114.833 | 118.518 | 209.912 | 5.259 |
| $KGeSe_3$ | 6.405 | 6.196 | 7.157 | 92.532 | 116.33 | 105.501 | 240.936 | 4.804 |
| $RbGeSe_3$ | 6.517 | 6.127 | 7.412 | 89.737 | 115.839 | 108.933 | 248.726 | 5.273 |
| $CsGeSe_3$ | 6.603 | 6.536 | 7.245 | 89.156 | 116.598 | 104.494 | 269.014 | 5.461 |
| $LiSnSe_3$ | 6.240 | 5.192 | 8.241 | 102.604 | 112.814 | 112.844 | 204.344 | 5.891 |
| $NaSnSe_3$ | 6.352 | 5.410 | 8.144 | 96.431 | 114.887 | 115.322 | 214.496 | 5.861 |
| $KSnSe_3$ | 6.434 | 5.848 | 7.986 | 89.083 | 116.404 | 110.644 | 248.337 | 5.278 |
| $RbSnSe_3$ | 6.664 | 6.550 | 7.472 | 97.489 | 114.526 | 106.341 | 273.139 | 5.362 |
| $CsSnSe_3$ | 6.733 | 6.437 | 7.792 | 88.384 | 116.098 | 109.081 | 283.970 | 5.712 |

**Table 2.** The Lattice parameters, unit cell volume, and theoretical density (D) of the studied perovskites using the HSE06 method.

Therefore, we can conclude that the above-mentioned perovskites have lower thermal conductivity compared to the other compounds.

## Electronic properties

*Band structures*

Figure 3 displays the predicted electronic band structures (BS) for the investigated Si-based, Ge-based, and Sn-based chalcogenide perovskites. The calculated bandgap ($E_g$) and the difference between indirect and direct gaps ($\Delta E_g$) for the investigated perovskites are summarized in Table 3. An indirect bandgap occurs when the maximum energy of the valence band (VB) and the minimum energy of the conduction band (CB) do not align at the same momentum (*k*-vector). This means that for an electron to transition from the VB to the CB, it must also interact with a phonon (a lattice vibration) to conserve momentum, making the process less efficient. This contrasts with direct bandgap materials, where such transitions can occur without the need for additional momentum exchange, allowing for more efficient photon absorption and emission. For solar cell applications, semiconductors with direct bandgaps are generally considered superior to those with indirect bandgaps. This is because direct bandgap materials exhibit significantly stronger optical absorption at the band edge due to the allowed momentum transitions between electrons and holes. Indirect semiconducting materials can also be efficient for solar cells, particularly when the $\Delta E_g$ falls within a specific range of approximately 0.2–0.5 eV[78]. A smaller $\Delta E_g$ in indirect bandgap semiconductors can potentially decrease electron–hole separation, avoiding fast recombination. According to recent research, the optimal band gap for solar cell applications should fall between 0.9 and 2.5 eV[31]. The BS reveal that all $ABSe_3$ perovskites exhibit semiconducting behavior with indirect bandgaps. In general, the $E_g$ increases with larger A-cations (Li to Cs) and follows the order Si > Sn > Ge for B-cations. The investigated perovskites exhibit indirect bandgaps within a range of 1.10–2.33 eV. This range indicates the tunability of the bandgap through compositional changes and is comparable to that of other perovskite structures and hybrid organic–inorganic compounds (Table 3). For instance, $CH_3NH_3PbI_3$ is a widely studied perovskite that has an indirect band gap of approximately 1.6 eV[79,80], which is within the range of the $ABSe_3$ perovskites. This material is known for its strong absorption properties and is a leading candidate for solar cell applications. Recent studies have also explored lead-free perovskites, such as $(C_6H_5NH_3)BiI_4$, which have band gaps around 2.14 eV[81]. These materials are being investigated for their potential in photovoltaic applications while avoiding the toxicity associated with lead. Materials like $YMnO_3$ and its derivatives have been reported to have band gaps around 1.35 eV[82], which is close to the lower end of the $ABSe_3$ perovskites' band gap range. These materials also show promise for solar cell applications due to their suitable band gap energies. Furthermore, the $ABSe_3$ possess a $\Delta E_g$ range of 0.149–0.493 eV, making them promising candidates for high-efficiency solar cell applications.

*Density of states*

The density of states (DOS) signifies the number of electronic states possible at each energy level for electrons in a material. The DOS provides a general overview of the electrical structure without specifying which atomic orbitals contribute to various states. In contrast, the partial density of states (PDOS) divides the overall DOS into contributions from individual atomic orbitals or atoms. This allows researchers to investigate how individual atomic qualities affect the material's electrical properties. The PDOS is derived by projecting the overall density of states onto specific atomic orbitals, such as *s*, *p*, or *d* orbitals, for each atom in the system, as shown in Fig. 4. Analysis of the PDOS of the VB of Li-based and K-based chalcogenides indicates that the states near the Fermi level (0 eV) down to − 10 eV are predominantly composed of Se-*p* states, with a moderate contribution from

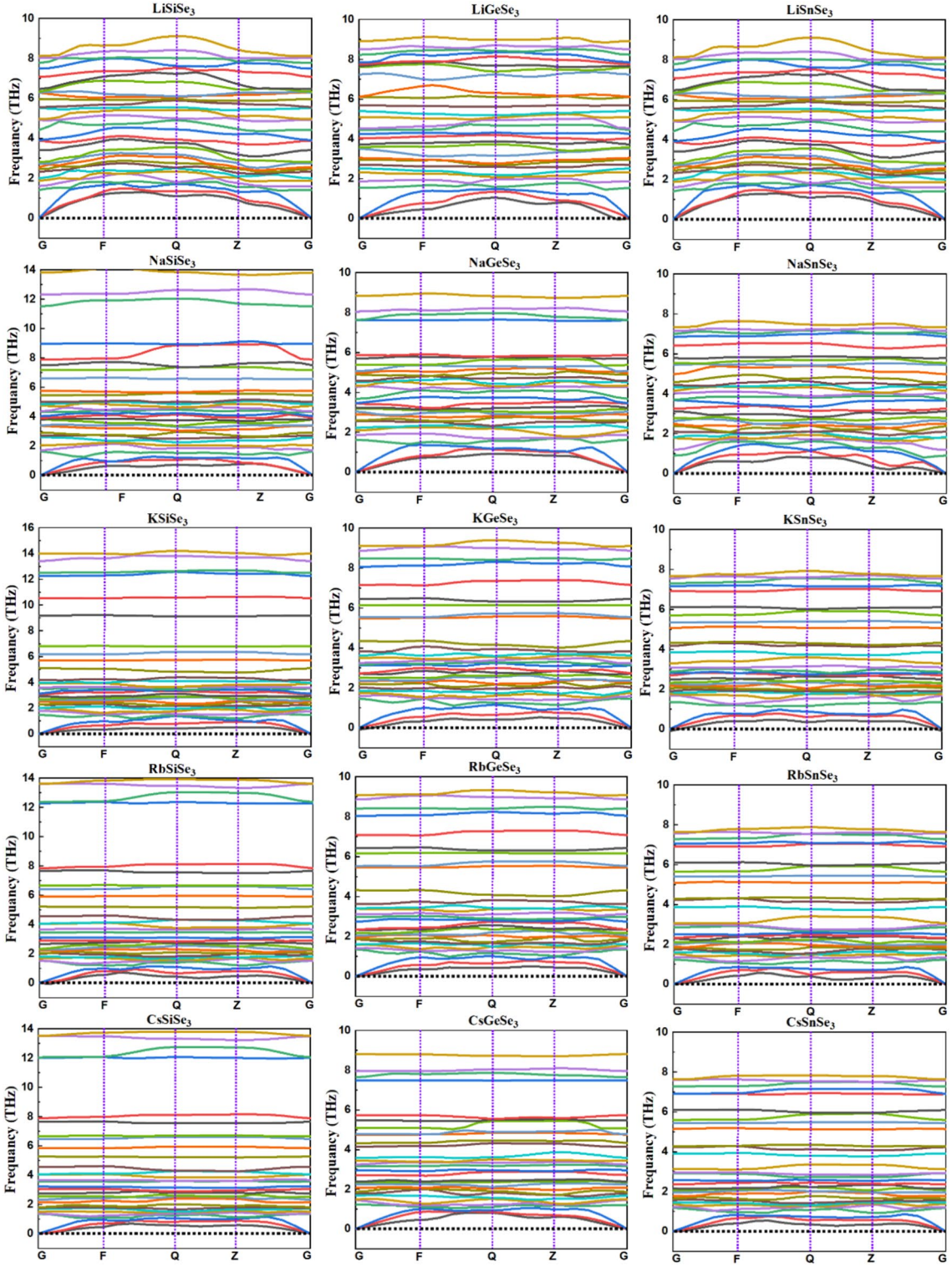


**Fig. 2.** Phonon dispersion curves for the chalcogenide perovskites $ABSe_3$ by using the GGA/PBEsol method.

B-*p* states. A smaller contribution is observed from A-*p* and Se-*s* states, while A-*s* and B-*s* states contribute minimally. For K-based, Rb-based, and Cs-based chalcogenides, the contributions remain predominantly from the transition Se-*p* electrons, with a small contribution from B-*p* electrons and a minor contribution of Se-*s* electrons. The A-cation *s* states reveal the consistent presence of sharp peaks at around – 55 eV for all compounds in Na-based chalcogenides, – 32 eV for all compounds in K-based chalcogenides, – 27 eV for all compounds in Rb-based chalcogenides, – 21 eV for all compounds in Cs-based chalcogenides. The A-cation p states exhibit sharp peaks around – 25 eV for all compounds in Na-based chalcogenides, – 15 eV for all compounds in K-based

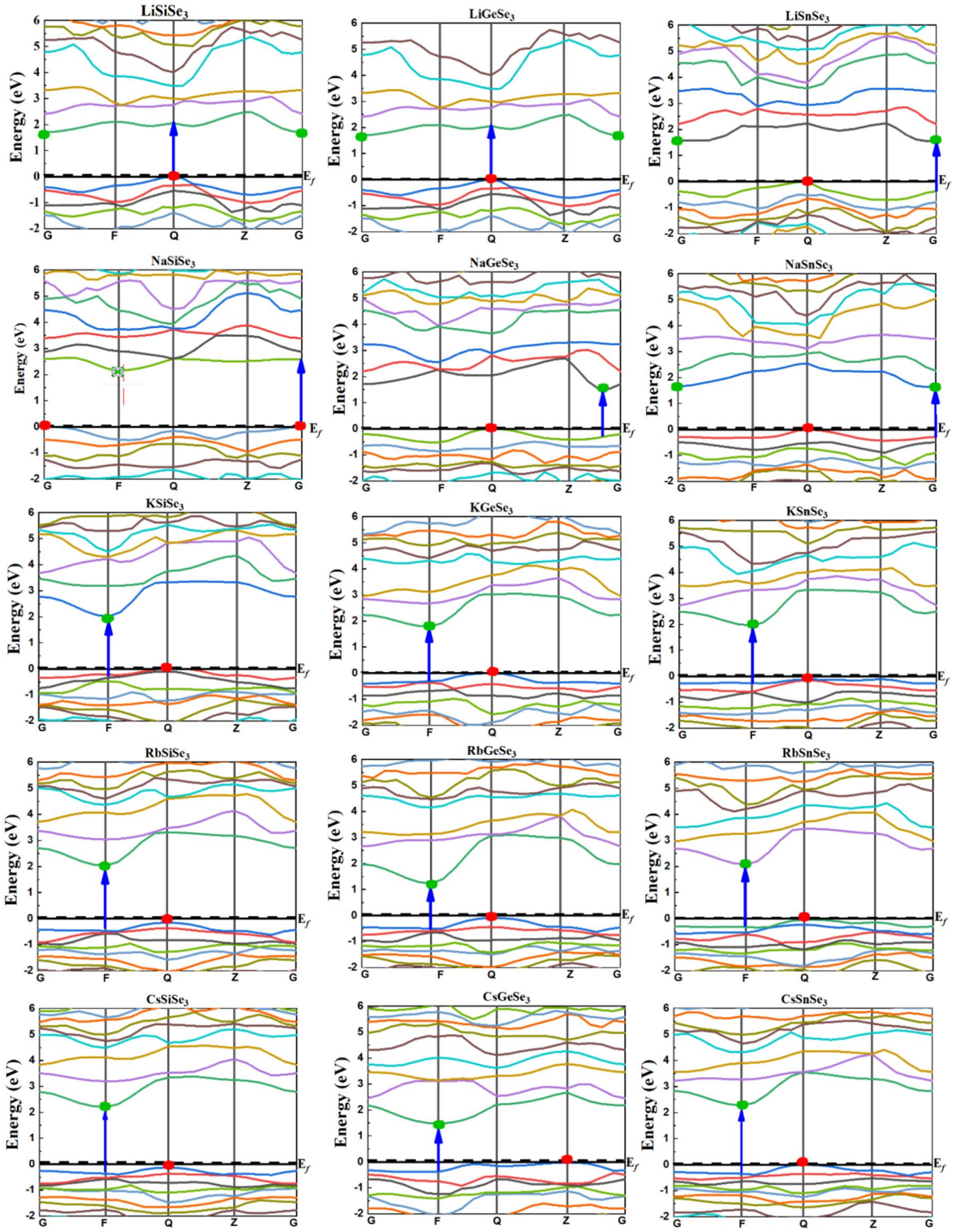


**Fig. 3.** Band structures curves for the $ABSe_3$ perovskites using the HSE06 method. The colored circles, red and green, on the highest valence and lowest conduction bands, represent the location of valance and conduction band edges, respectively. The blue arrow indicates the onset of the direct band.

chalcogenides, – 12 eV for all compounds in Rb-based chalcogenides, – 8 eV for all compounds in Cs-based chalcogenides. The states at the bottom of the CB are mainly due to the Se-*p* states. Analysis of the K-based, Rb-based, and Cs-based chalcogenides reveals that the *d* states of the A-cation exhibit broad peaks within the CB, ranging approximately from 3 to 18 eV.

| Perovskite | $E_g$ | $\Delta E_g$ | $E_g$ type | Ref | Perovskite | $E_g$ | Method | $E_g$ type | Refs. |
|---|---|---|---|---|---|---|---|---|---|
| $LiSiSe_3$ | 1.69 | 0.405 | Indirect | This work | $(CH_3NH_3)PbI_3$ | 1.6 | Exp. | Indirect | [79,80] |
| $NaSiSe_3$ | 2.15 | 0.493 | Indirect | This work | $(C_6H_5NH_3)BiI_4$ | 2.14 | Exp. | Direct | [81] |
| $KSiSe_3$ | 2.01 | 0.228 | Indirect | This work | $YMnO_3$ | 1.35 | Exp. | Direct | [82] |
| $RbSiSe_3$ | 2.18 | 0.317 | Indirect | This work | $CaSnS_3$ | 1.40 | HSE06 | Direct | [34] |
| $CsSiSe_3$ | 2.33 | 0.265 | Indirect | This work | $BaHfS_3$ | 1.97 | HSE06 | Direct | [34] |
| $LiGeS_3$ | 1.10 | 0.237 | Indirect | This work | $CaHfS_3$ | 2.23 | HSE06 | Direct | [34] |
| $NaGeSe_3$ | 1.45 | 0.189 | Indirect | This work | SrHfS3 | 2.32 | HSE06 | Direct | [34] |
| $KGeSe_3$ | 1.78 | 0.311 | Indirect | This work | $Ba_2CdS_3$ | 2.56 | HSE06 | Direct | [83] |
| $RbGeSe_3$ | 1.32 | 0.418 | Indirect | This work | $Ba_2CdSe_3$ | 2.16 | HSE06 | Direct | [83] |
| $CsGeSe_3$ | 2.21 | 0.331 | Indirect | This work | $Ba_2CdTe_3$ | 3.16 | HSE06 | Direct | [83] |
| $LiSnS_3$ | 1.55 | 0.371 | Indirect | This work | $Ba_6CS_4$ | 1.554 | HSE06 | Direct | [84] |
| $NaSnSe_3$ | 1.63 | 0.288 | Indirect | This work | $Ba_6CSe_4$ | 1.311 | HSE06 | Direct | [84] |
| $KSnSe_3$ | 2.06 | 0.149 | Indirect | This work | $Ba_6CTe_4$ | 1.517 | HSE06 | Direct | [84] |
| $RbSnSe_3$ | 2.11 | 0.278 | Indirect | This work | $SrZrS_3$ | 2.009 | TB-mBJ | Direct | [41] |
| $CsSnSe_3$ | 2.27 | 0.352 | Indirect | This work | $SrZrSe_3$ | 1.096 | TB-mBJ | Direct | [41] |
| | | | | | BaZrS3 | 1.770 | TB-mBJ | Direct | [42] |
| | | | | | BaZrSe3 | 1.250 | TB-mBJ | Direct | [42] |

**Table 3.** The $E_g$ and $\Delta E_g$ values of the studied perovskites using the HSE06 method compared with similar published perovskites.

## Optical properties

The optical properties of perovskites play a critical role in understanding their internal structures. The dielectric function, ε(ω), characterizes the interaction of an electromagnetic wave with a material as a function of frequency (ω). It describes how the material polarizes in response to the electric field of the wave. Furthermore, the dielectric function can also provide insights into the interactions between electrons and phonons within the material. The real part of the complex dielectric function, $\varepsilon_1(\omega)$, reflects the polarization induced in the material by the propagating light wave. While, the imaginary part, $\varepsilon_2(\omega)$, quantifies the energy absorbed by the material due to the interaction with the electromagnetic wave. Determination of the $\varepsilon_1(\omega)$ and $\varepsilon_2(\omega)$ allows us to calculate other optical properties like absorption, refractive index, dielectric function, conductivity, reflectivity, and energy loss. The $\varepsilon_1(\omega)$ and $\varepsilon_2(\omega)$ parts of dielectric constants are shown in Fig. 5. The $\varepsilon_1(\omega)$ of $LiSiSe_3$, $NaSiSe_3$, $KSiSe_3$, $RbSiSe_3$ and $CsSiSe_3$ at a photon energy of 0.01 are 7.08, 5.91, 5.43, 5.39, and 5.35, respectively (Fig. 5a). The $\varepsilon_1(\omega)$ at a photon energy of 0.01 for $LiGeSe_3$, $NaGeSe_3$, $KGeS_3$, $RbGeSe_3$ and $CsGeSe_3$ are 8.930, 7.895, 6.085, 5.885, and 5.130, respectively (Fig. 5b). The $\varepsilon_1(\omega)$ values at photon energy of 0.01 for $LiSnSe_3$, $NaSnSe_3$, $KSnSe_3$, $RbSnSe_3$ and $CsSnSe_3$ are 6.789, 6.278, 5.160, 5.009 and 4.946, respectively (Fig. 5c). From the $\varepsilon_1(\omega)$ values of Si-based, Ge-based, and Sn-based chalcogenides, we observe that the maximum $\varepsilon_1(\omega)$ value decreases upon moving cation A from Li to Cs, which could be related to the increasing atomic size and decreasing electronegativity of the alkali metals. Comparing the three groups (Si, Ge, Sn) indicates how replacing Si with Ge or Sn alters the dielectric response. Ge-containing materials generally have higher $\varepsilon_1(\omega)$ values than their Si and Sn counterparts, indicating a stronger dielectric response, which might be crucial in applications where Ge is preferred for its superior electronic properties. Among the Si-based and Sn-based perovskites, the materials containing Li and Na exhibit higher values of the $\varepsilon_1(\omega)$. Materials with high $\varepsilon_1(\omega)$ at low energies are often more suitable for applications in optoelectronic devices, where a high dielectric constant is desirable for efficient charge separation and transport. $LiGeSe_3$ and $NaGeSe_3$ exhibit the highest $\varepsilon_1(\omega)$ values at lower energies ~ (0.01 to 5.0) eV. Therefore, $LiGeSe_3$ and $NaGeSe_3$ exhibit competitive $\varepsilon_1(\omega)$ values compared to traditional (~ 11.7 for silicon[85], 9.5 for CdTe[86]) and emerging materials (~ 6.5 for $CH_3NH_3PbI_3$[87]), suggesting their potential for effective use in solar cells, albeit with considerations for stability, cost, and scalability. For most Si-based, Ge-based, and Sn-based chalcogenides, $\varepsilon_1(\omega)$ remains positive up to approximately 7.48–7.91 eV, 6.43–7.81 eV, and 7.15–7.95 eV, respectively. The ability to maintain positive $\varepsilon_1(\omega)$ at high energies means these materials are less likely to exhibit significant optical absorption losses in the visible and near-UV regions, which can enhance their performance in optoelectronic devices. The $\varepsilon_2(\omega)$ starts increasing from zero at around 1.8 eV, which is an absorption edge and reaches its maximum value around 7.8 eV, which reveals that the absorption is maximum in the ultra-violet region.

The refractive index $n(\omega)$ indicates the amount of light refracted or bent, when entering a material. Figure 6a–c represents the refractive index (real part) for (a) Si-based (b), Ge-based, and (c) Sn-based chalcogenides. Figure 6a depicts that $LiSiSe_3$, $NaSiSe_3$, $KSiSe_3$, $RbSiSe_3$ and $CsSiSe_3$ have $n(\omega)$ of ~ 2.661, 2.432, 2.330, 2.323, and 2.318 at photon energy of 0.01, respectively. From Fig. 6b, the $n(\omega)$ for $LiGeSe_3$, $NaGeSe_3$, $KGeS_3$, $RbGeSe_3$ and $CsGeSe_3$ are 2.989, 2.809, 2.466, 2.425 and 2.475, respectively. The $n(\omega)$ values for $LiSnSe_3$, $NaSnSe_3$, $KSnSe_3$, $RbSnSe_3$, and $CsSnSe_3$ are 2.605, 2.505, 2.271, 2.238 and 2.224, respectively (Fig. 6c). For each group (Si, Ge, Sn), the refractive index generally decreases as the cation size increases from Li to Cs. This trend suggests that larger cations lead to a lower refractive index, likely due to changes in lattice parameters and bonding characteristics. The Ge-based chalcogenides exhibit the highest refractive indices compared to Si and Sn-based materials. A higher refractive index can improve light trapping within the solar cell by increasing the likelihood

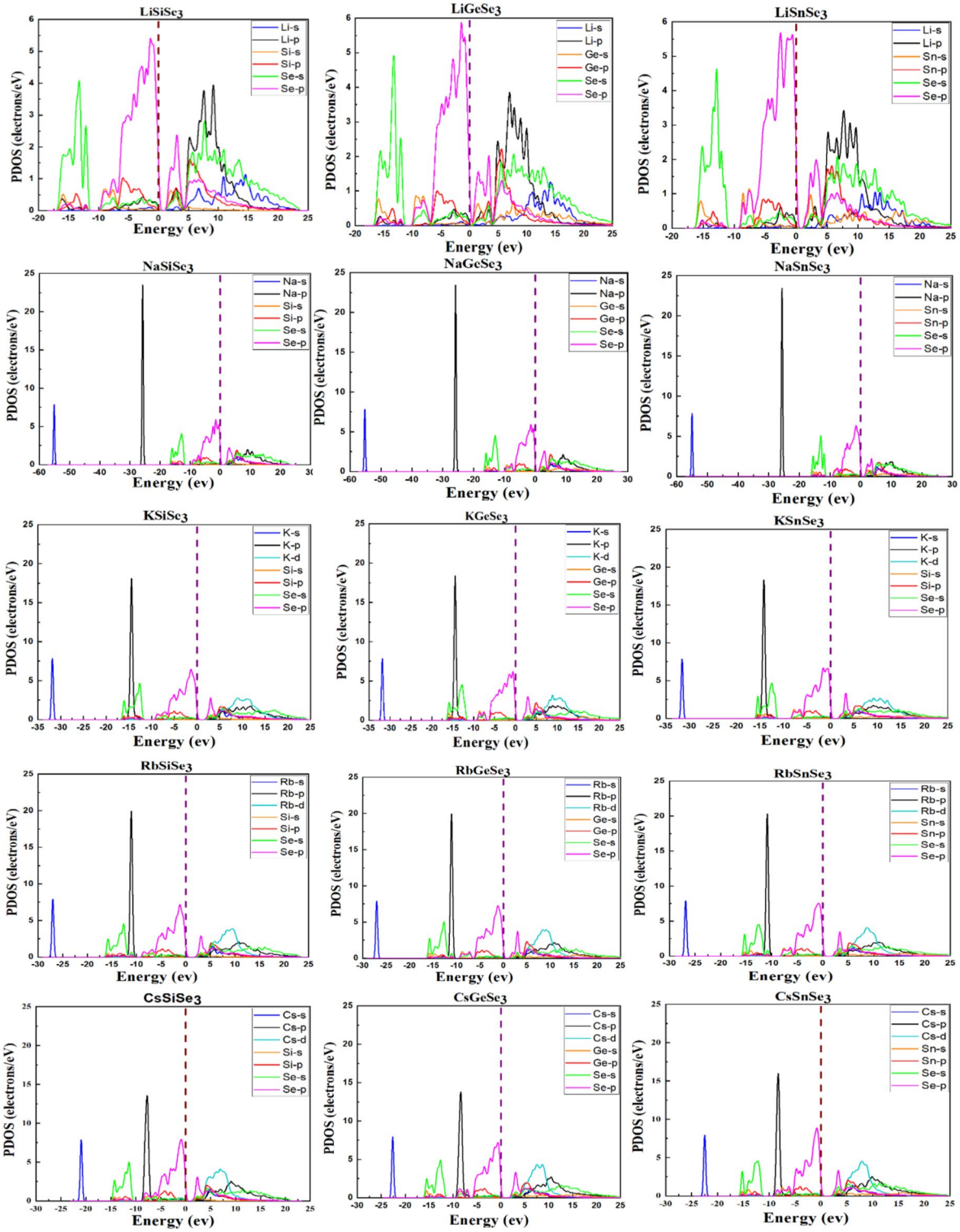


**Fig. 4.** The calculated PDOS of $ABSe_3$ perovskites using the HSE06, the maroon vertical dashed line represents the Fermi level ($E_F$), the reference point with zero energy.

of light being reflected and scattered within the active layer. This can enhance the absorption of light, especially in thin-film solar cells where the thickness of the absorbing material is limited. Given that $LiGeSe_3$ and $NaGeSe_3$ have the highest refractive indices among the materials listed, with values of 2.989 and 2.809 respectively. They are comparable to Si (~ 3.5)[88] or slightly higher than CdTe (~ 2.6)[89] and perovskites ($CH_3NH_3PbI_3$, ~ 2.5–3.0)[90]. This suggests they are competitive with these well-known materials in terms of light interaction, which is significant for solar cell and optoelectronic applications. Figure 7a–c represents the extinction coefficient, $k(\omega)$, the imaginary part of the complex refractive index, for (a) Si-based, (b) Ge-based, and (c) Sn-based chalcogenides.

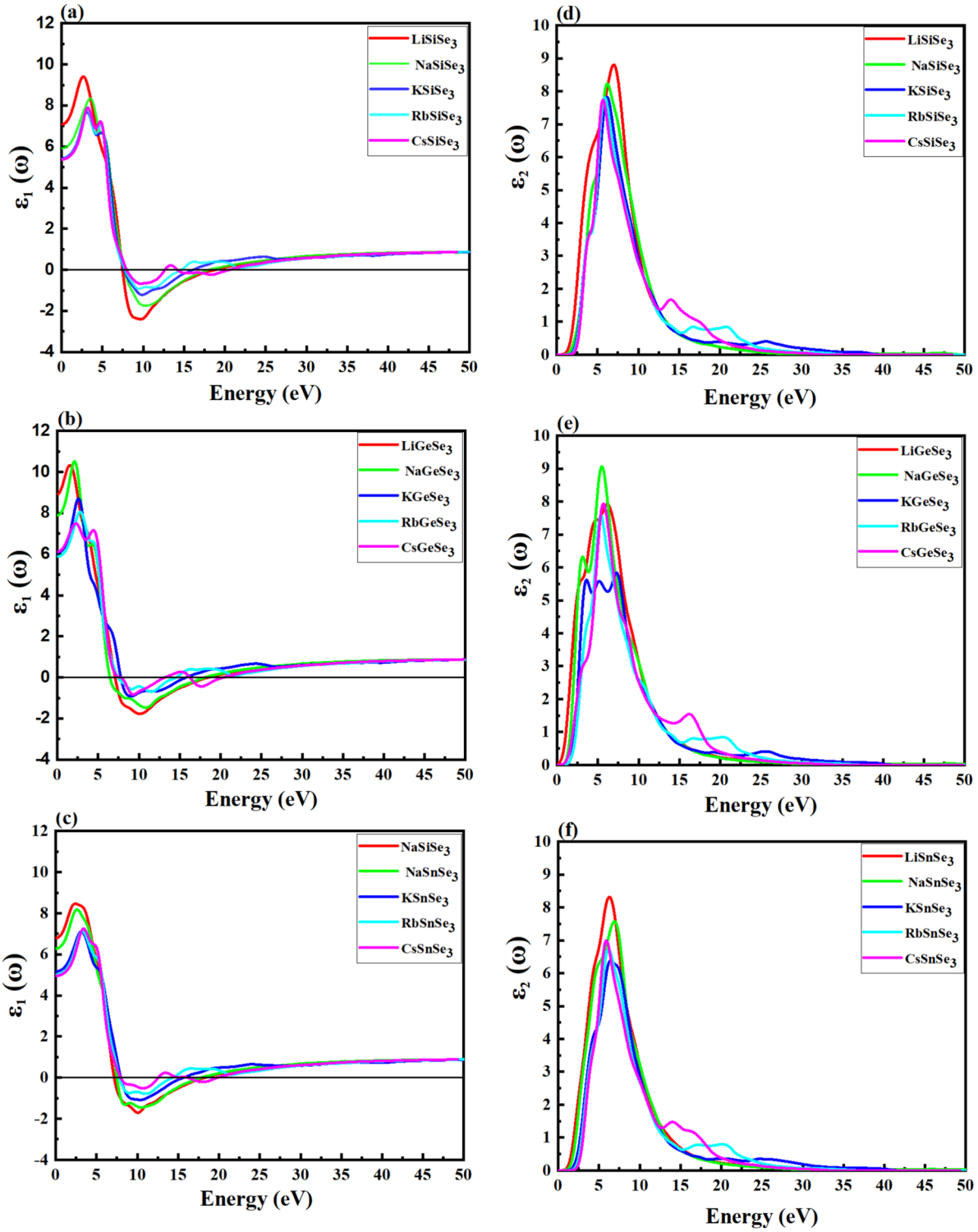


**Fig. 5.** The calculated real dielectric, $\varepsilon_1(\omega)$, of (**a**) Si-based, (**b**) Ge-based, and (**c**) Sn-based chalcogenide perovskites using the HSE06; the imaginary dielectric, $\varepsilon_2(\omega)$, of (**d**) Si-based, (**e**) Ge-based, and (**f**) Sn-based perovskites.

It represents the attenuation or absorption of light as it propagates through a material. The local maxima peak of the $k(\omega)$ for our study perovskites centered around 8.0 eV. It is noted that Si-based chalcogenides exhibit the highest $k(\omega)$ compared with Ge-based and Si-based ones. Generally, the Li and Na-based chalcogenides tend to display higher values of the $n(\omega)$ and $k(\omega)$ compared to other materials in the same category.

Figure 8 shows the absorption coefficient $\alpha(\varepsilon)$ of chalcogenide perovskites. Within the 2–15 eV energy region, the absorption coefficient progressively decreases as the A-cation changes from Li to Cs. In the higher energy

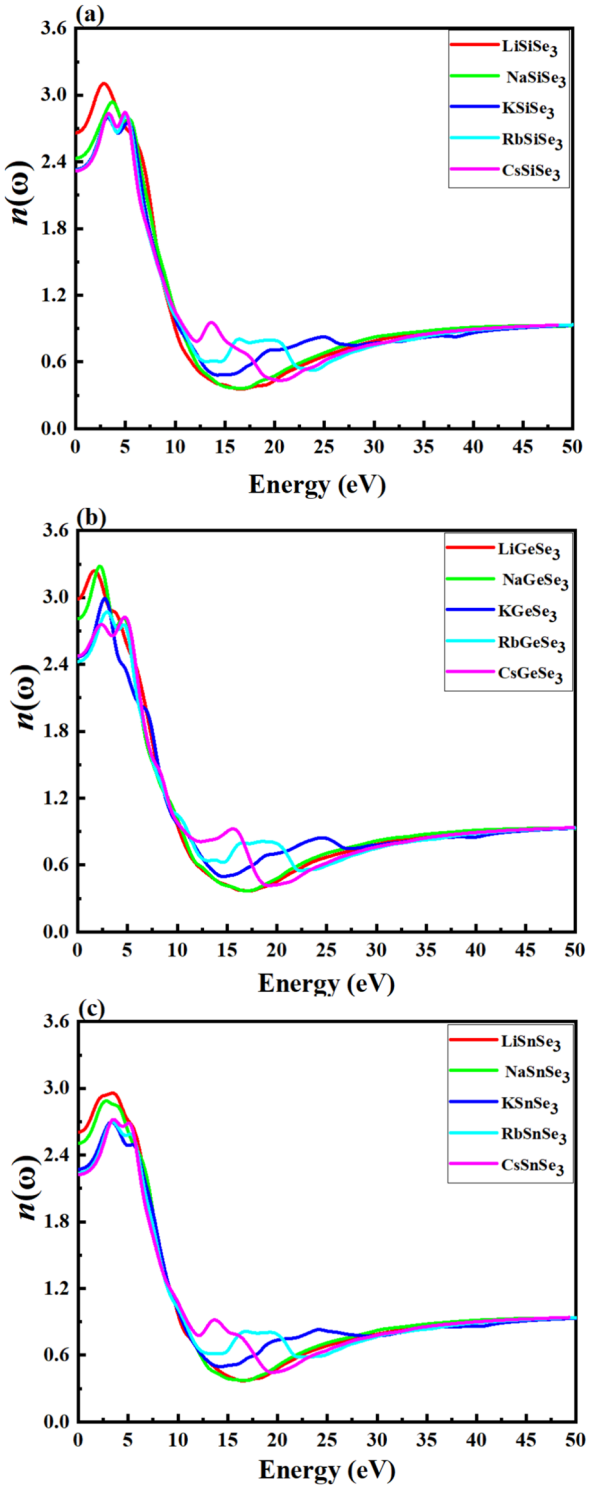


**Fig. 6.** Calculated refractive index of (**a**) Si-based, (**b**) Ge-based, and (**c**) Sn-based chalcogenide perovskites using the HSE06 method.

region (15 eV to 45 eV), the absorption coefficient slightly increases as the A-cation moves from K to Cs. Across the 2–45 eV energy range, the absorption coefficient generally decreases as the B-cation changes from Si to Sn. Notably, all the studied chalcogenide perovskites exhibit strong absorption in the UV region.

The complex conductivity, σ(ω), describes the conduction of electrons due to an applied electromagnetic field. It is a complex function consisting of both real, $\sigma_1(\omega)$, and imaginary component, $\sigma_2(\omega)$. The $\sigma_1(\omega)$ indicates how effectively a material can conduct electricity when subjected to electromagnetic radiation. Figure 9a–c illustrates the computed $\sigma_1(\omega)$ spectra for studied perovskites at incoming photon energy ranging from 0 to 50 eV. All

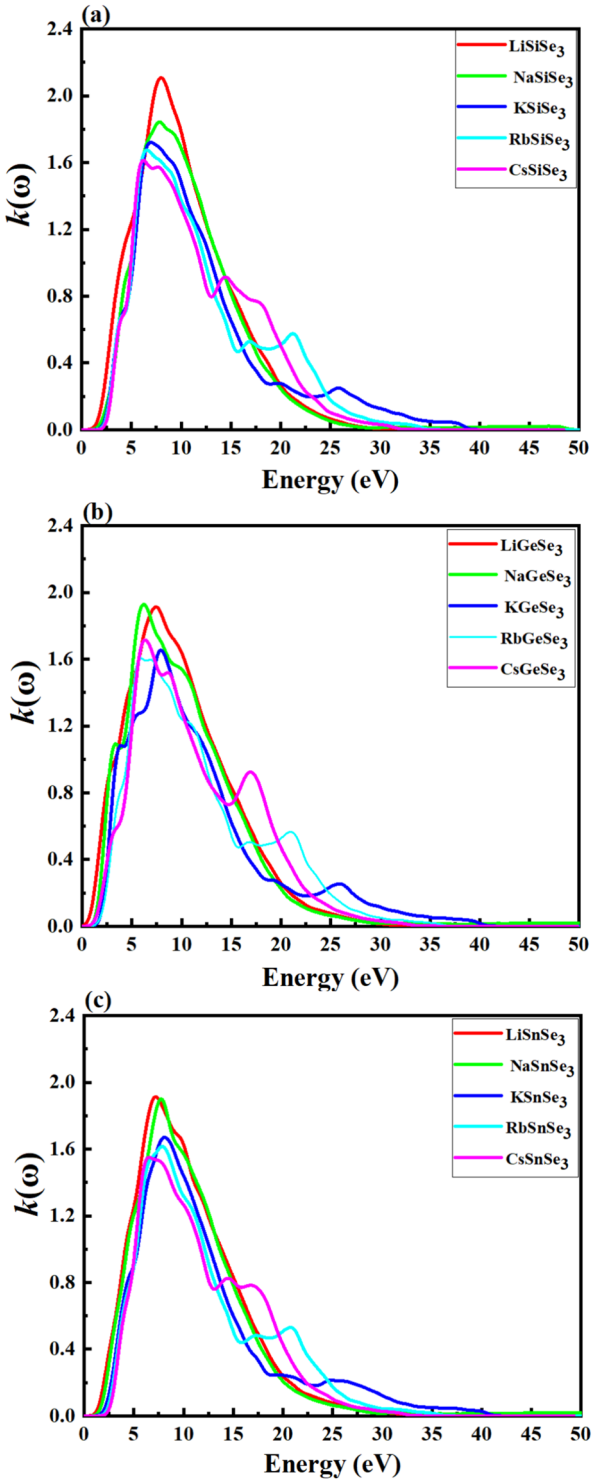


**Fig. 7.** Calculated extinction coefficient of (**a**) Si-based, (**b**) Ge-based, and (**c**) Sn-based chalcogenide perovskites using the HSE06.

$ABSe_3$ materials have a maximum $\sigma_1(\omega)$ within the range of ~ 1–15 eV of photon energy, which is promising for their application in UV optical systems. This concurrence suggests that light absorption leads to the generation of free carriers, which in turn contribute to electrical conductivity. In this energy range, the $\sigma_1(\omega)$ primarily corresponds to transitions involving Se-*p* electron with a moderate contribution of B-*p*, small of A-*p*, Se-*s*, and a minor contribution of A-*s* and B-*s* electrons for Li-based and Na-based chalcogenides. For K-based, Rb-based, and Cs-based chalcogenides, the contributions to the $\sigma_1(\omega)$ remain predominantly from the transition Se-*p* electrons, with a small contribution from B-*p* electrons and a minor contribution of Se-*s* electrons. High $\sigma_1(\omega)$

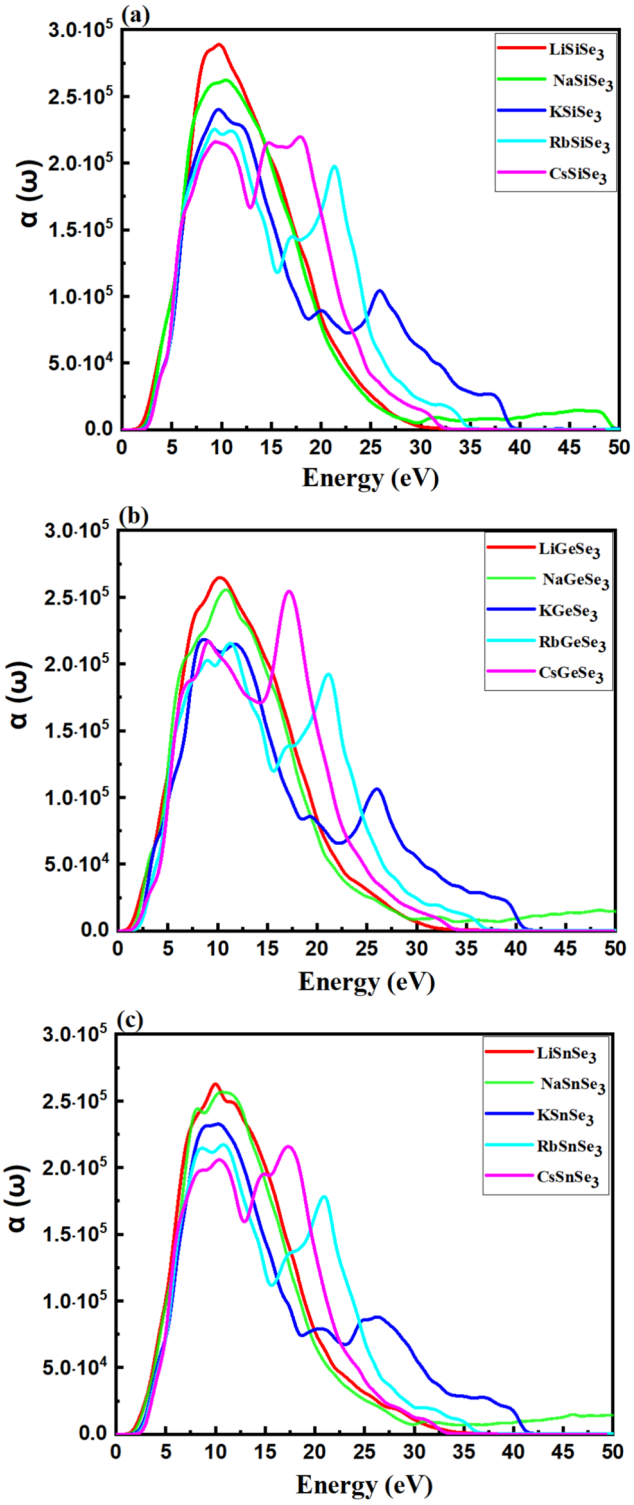


**Fig. 8.** Calculated absorption coefficient of (**a**) Si-based, (**b**) Ge-based and (**c**) Sn-based perovskites.

peaks were observed at ~ 16, 20, and 25 eV mainly corresponding to transitions concerning Se-p electron Ce-p, Rb-p, and K-p, respectively. Consistent with the absorption trends, the magnitude of the $\sigma_1(\omega)$ spectra is higher for Si-based chalcogenide perovskites compared to Ge-based and Sn-based perovskites. The $\sigma_2(\omega)$ represents the reactive component of the conductivity, which to the storage of energy in the material. The $\sigma_2(\omega)$ curves extend from 0 eV incident photon energy up to 50 eV. At around 0 eV to 7 eV input photon energy, $ABSe_3$ reach negative maximum values of about (− 3.14, − 3.489, − 3.480, − 3.619 and − 3.651) 1/*fs* for $LiSiSe_3$, $NaSiSe_3$, $KSiSe_3$, $RbSiSe_3$ and $CsSiSe_3$ respectively (Fig. 9d). Negative maximum $\sigma_2(\omega)$ values for $LiGeSe_3$, $NaGeSe_3$, $KGeSe_3$, $RbGeSe_3$, and

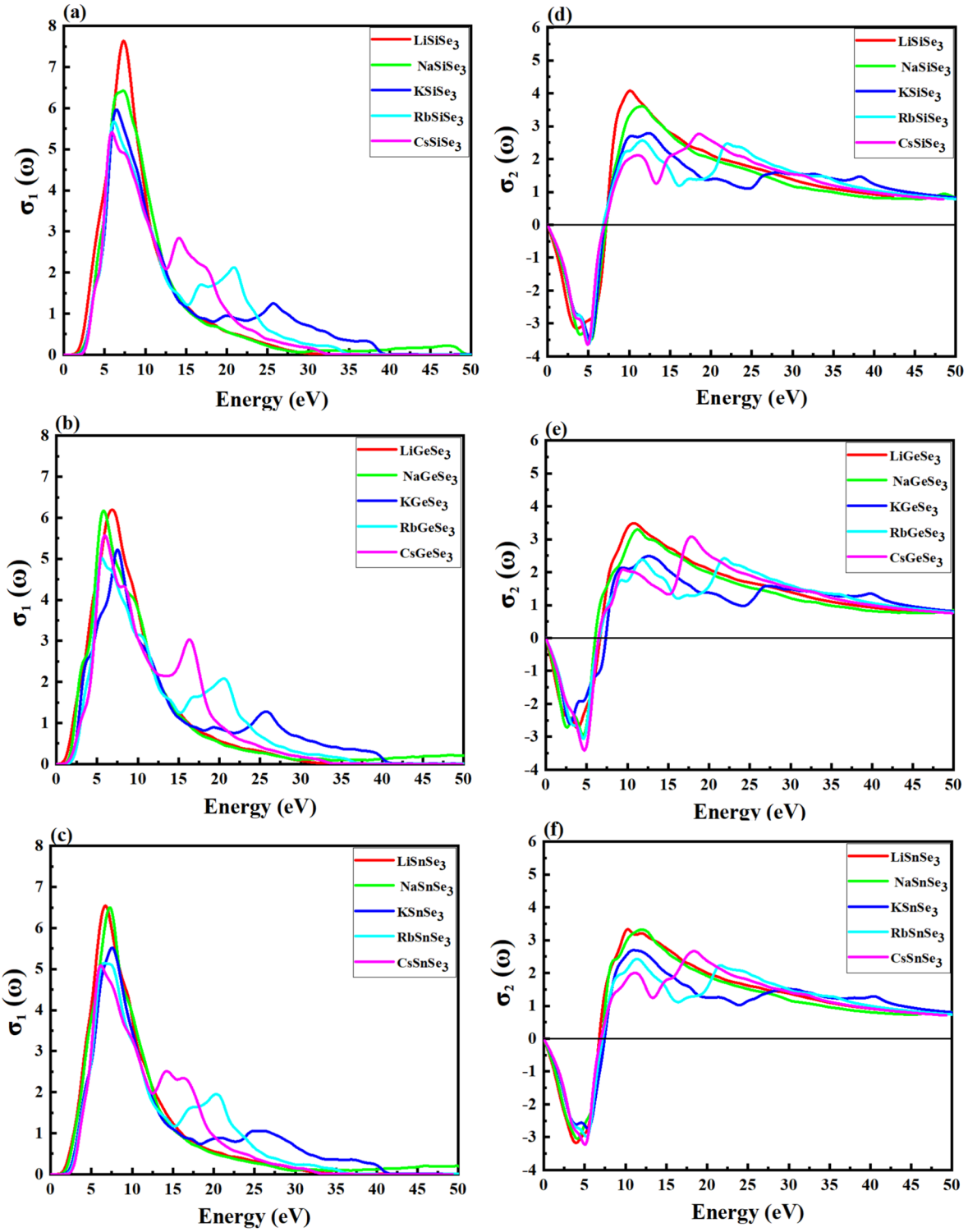


**Fig. 9.** The calculated real part of optical conductivity for (**a**) Si-based, (**b**) Ge-based, and (**c**) Sn-based perovskites using the HSE09 method; the imaginary part of optical conductivity, (**d**) Si-based, (**e**) Ge-based, and (**f**) Sn-based perovskites.

$CsGeSe_3$ were obtained at around − 2.733, − 2.947, − 3.00, − 3.074, and − 3.407 1/*fs*, respectively (Fig. 9e). Figure 9f reveals that for $LiSnSe_3$, $NaSnSe_3$, $KSnSe_3$, $RbSnSe_3$ and $CsSnSe_3$ negative maximum $\sigma_2(\omega)$ values at around − 3.170, − 3.045, − 2.741, − 2.996 and − 3.249 respectively. The negative maximum values of $\sigma_2(\omega)$ in chalcogenide perovskites significantly impact their overall conductivity by reducing it and indicating a capacity for energy storage. The larger negative values in chalcogenide perovskites indicate that these materials may be more effective for applications requiring efficient energy storage and conversion, such as in solar cells. At around 7 eV to 15

eV input photon energy, Si-based, Ge-based, and Sn-based perovskites maximum positive of $\sigma_2$ (ω) about range (2–4), (2.1–3.5) and (1.85–3.2) 1/*fs*. The shift to positive $\sigma_2(\omega)$ values implies that charge carriers (electrons) are becoming more mobile and contributing to the conduction process.

The reflectivity, $R(\omega)$, mainly measures the ability of a material to reflect incident light. Figure 10a–c depicts the $R(\omega)$ values for $ABSe_3$ at a photon energy of 0.01 eV. The $R$ (ω) values for $LiSiSe_3$, $NaSiSe_3$, $KSiSe_3$, $RbSiSe_3$, and $CsSiSe_3$ are ~ 0.205, 0.174, 0.159, 0.158, and 0.157, respectively (Fig. 10a). Similarly, for $LiGeSe_3$, $NaGeSe_3$,

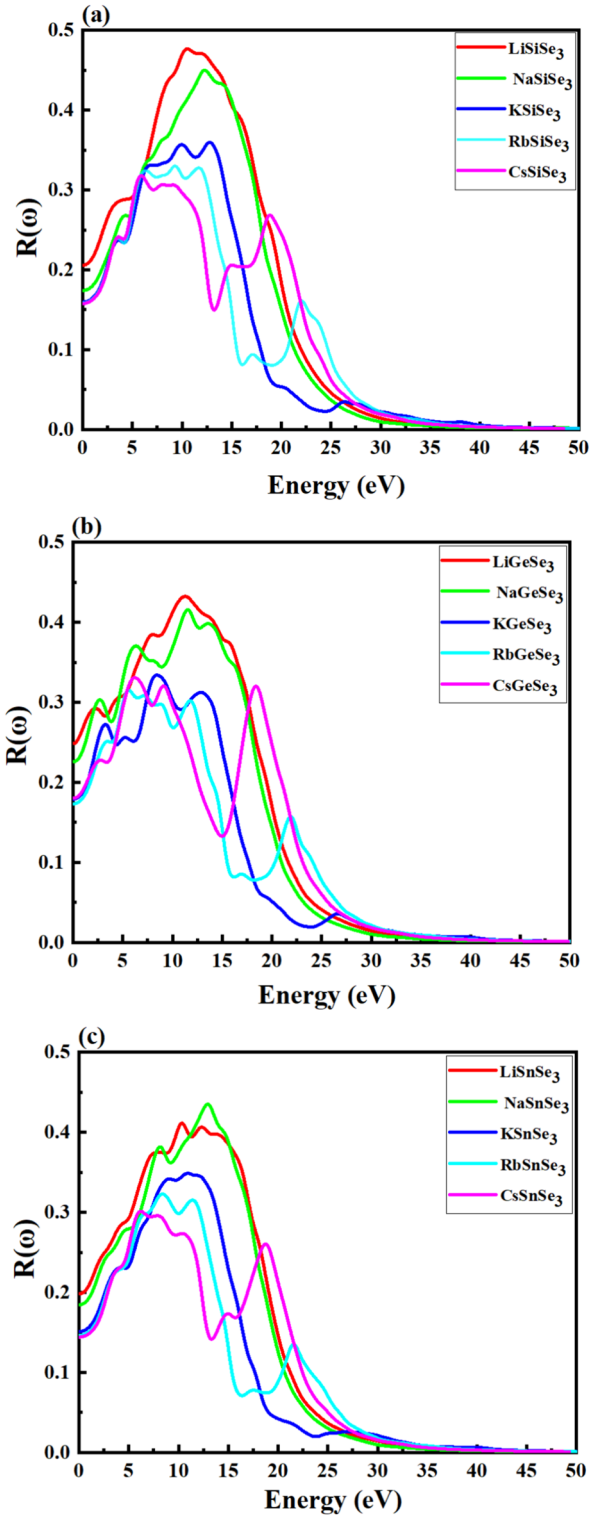


**Fig. 10.** Reflectivity spectra of (**a**) Si-based, (**b**) Ge-based, and (**c**) Sn-based perovskites using the HSE06 method.

$KGeSe_3$, $RbGeSe_3$, and $CsGeSe_3$, the R(ω) values are 0.248, 0.225, 0.179, 0.173, and 0.180, respectively (Fig. 10b). Finally, Fig. 10c shows that the R(ω) values for LiSnSe3, $NaSnSe_3$, $KSnSe_3$, $RbSnSe_3$, and $CsSnSe_3$ are 0.198, 0.184, 0.151, 0.146, and 0.144, respectively. For efficient solar cells, lower reflectivity is desirable because it means that more incident light is absorbed rather than reflected. Across all groups (Si-based, Ge-based, and Sn-based), the reflectivity $R(\omega)$ generally tends to decrease as we move from Li-based to Cs-based chalcogenides. This trend suggests that as the atomic number of the A cation increases, the material becomes slightly more transparent or less reflective at the given photon energy (0.01 eV). Among the different groups, Ge-based chalcogenides generally exhibit higher reflectivity values than Si-based and Sn-based chalcogenides, at 0.01 eV. This implies that Ge-based chalcogenides may reflect more light, which could reduce their effectiveness in absorbing photons and thus converting them into electrical energy in solar cell applications. Materials like $CsSnSe_3$, which have the lowest reflectivity (~ 0.144), are therefore more favorable for solar cell applications as they would absorb lighter and potentially generate more electricity. While the Ge-based $ABSe_3$ chalcogenides show slightly higher reflectivity, they still fall within a reasonable range that could be optimized through material engineering (e.g., surface texturing, anti-reflective coatings) for better solar cell performance. The reflectivity of the $ABSe_3$ materials, particularly the Sn-based compounds, is comparable to or lower than that of some well-known materials used in thin-film solar cells, such as $Cu_2ZnSnS_4$ (20–25% in the visible spectrum)[91], $SrTiO_3$ (R around 20–30% in the visible spectrum)[92], and $CH_3NH_3PbI_3$ (5–15% in the visible spectrum)[93]. This low reflectivity makes $ABSe_3$ materials potential candidates for solar applications. The reflectivity is more significant in the range of 1.2 eV to 35 eV and becomes negligible at above 45 eV.

The electron loss energy, L(ω), partly describes the energy loss due to fast-moving electrons through the lattice. Figure 11 reveals that for the perovskite materials, L(ω) is zero for photon energies between 0 and 4.48 eV. In Fig. 11a, a sharp peak is found at 19.5, 18.9, 16.7, 23.9 and 21.5 eV for $LiSiSe_3$, $NaSiSe_3$, $KSiSe_3$, $RbSiSe_3$ and $CsSiSe_3$, respectively. Figure 11b also exhibits sharp peaks in the L(ω) spectra for Ge-based perovskites. The peak positions show variations across the A-cation (Li, Na, K, Rb, Cs), with values of 19.4, 18.6, 16.8, 22.8, and 21.4 eV, respectively. Similarly, the specific peak positions for $LiSnS_3$, $NaSnS_3$, $KSnS_3$, $RbSnS_3$, and $CsSnS_3$ are 18.9, 18.7 eV, 16.4 eV, 22.8 eV, and 20. 8 eV, respectively (Fig. 11c). The $LiSiS_3$, $LiGeS_3$ and $LiSnS_3$ perovskites show highest L(ω) values, while $KSiS_3$, $KGeS_3$, and $RbSnS_3$ show lowest peaks compared to the others perovskites.

## Conclusions

This study employs density functional theory calculations to comprehensively investigate the structural, electronic, and optical properties of triclinic chalcogenide perovskites, $ABSe_3$ (A = Li, Na, K, Rb, Cs; B = Si, Ge, Sn). Our findings reveal several important insights: Firstly, the tolerance factor and negative formation energy values suggest that these compounds exhibit both thermodynamic and structural stability, indicating their potential for practical applications. Secondly, the absence of imaginary phonon modes in the phonon dispersion curves confirms the dynamical stability of $ABSe_3$ perovskites, eliminating concerns about structural instability in practical applications. Thirdly, examination of the band structures indicates all studied perovskites exhibit favorable indirect band gaps (1.10–2.33 eV) with a small difference from direct gaps (0.149–0.493 eV), providing potential applications, particularly in photovoltaics. A larger A-cation (Li to Cs) generally leads to a wider band gap, while for B-cations, $E_g$ follows the order Si > Sn > Ge. Finally, the predicted optical properties of the proposed chalcogenide perovskites are comparable to some of the traditional and emerging materials. $LiGeSe_3$ and $NaGeSe_3$ exhibit the highest $\varepsilon_1(\omega)$ values at lower energies ~ (0.01 to 5.0) eV. Therefore, $LiGeSe_3$ and $NaGeSe_3$ exhibit competitive ε1(ω) values compared to traditional (Si, CdTe) and emerging materials (e.g., $CH_3NH_3PbI_3$). They also have the highest $n(\omega)$ among the $ABSe_3$ materials listed, with close to Si and slightly higher than CdTe and $CH_3NH_3PbI_3$. The $ABSe_3$ materials exhibit a high absorption coefficient within the energy range of ~ 2–15 eV, and their reflectivity, particularly the Sn-based compounds (e.g., $CsSnSe_3$), are comparable to or lower than that of some well-known materials used in thin-film solar cells, such as $Cu_2ZnSnS_4$, $SrTiO_3$, and $CH_3NH_3PbI_3$. The properties suggest $ABSe_3$ could be promising candidate materials for solar cell applications. Future research should focus on experimentally validating the predicted properties of $ABSe_3$ perovskites through synthesis, characterization, and optical/electronic measurements. Exploring other compositions, such as doping and mixed systems, could further optimize their properties. Additionally, simulating and developing prototypes for photovoltaic devices will help assess the real-world efficiency of these materials. Finally, studying their environmental stability and toxicity is crucial for ensuring safe and practical applications.

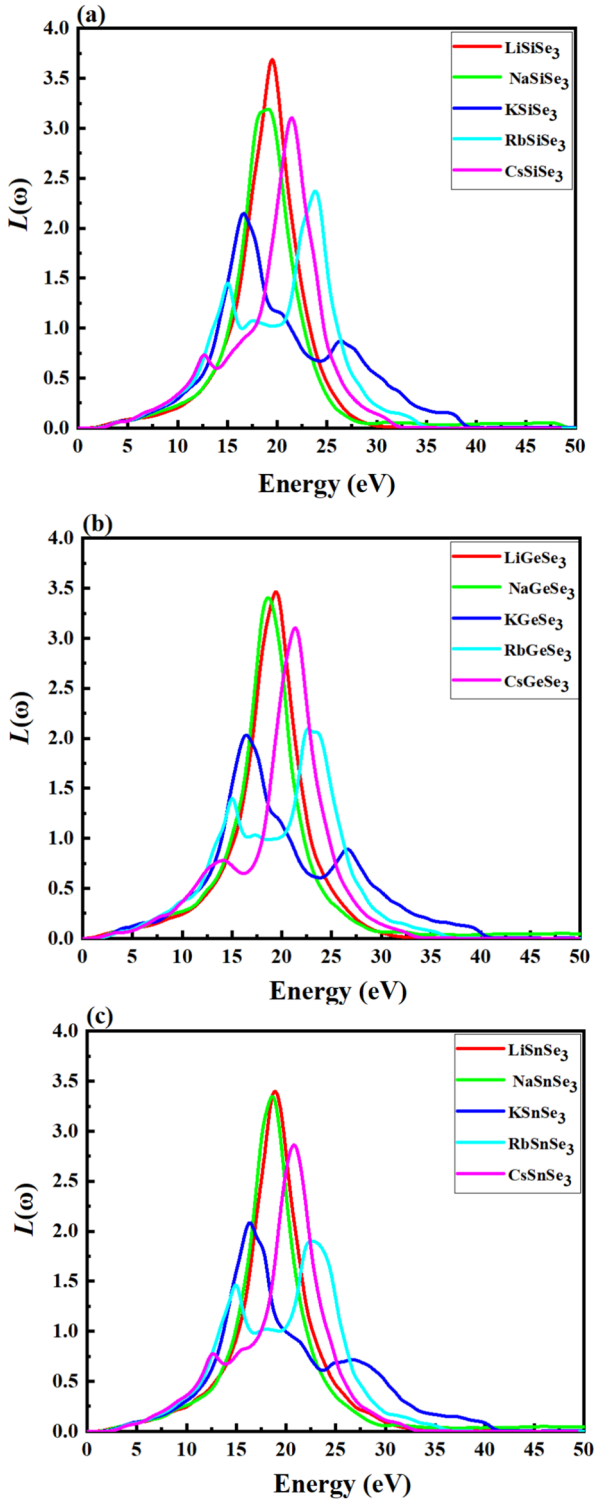


**Fig. 11.** The optical loss function of (**a**) Si-based, (**b**) Ge-based, and (**c**) Sn-based perovskites using the HSE06 method.

## Data availability

All data generated or analysed during this study are included in this published article.

Received: 22 June 2024; Accepted: 9 September 2024
Published online: 30 September 2024

## References


1. Jana, M. K. *et al.* Direct-bandgap 2D silver–bismuth iodide double perovskite: The structure-directing influence of an oligothiophene spacer cation. *J. Am. Chem. Soc.* **141**(19), 7955–7964 (2019).
2. Yang, J., Zhang, P. & Wei, S. H. Band structure engineering of Cs2AgBiBr 6 perovskite through order–disordered transition: A first-principle study. *J. Phys. Chem. Lett.* **9**(1), 31–35 (2018).
3. Xiao, Z. *et al.* Intrinsic instability of Cs2In (I) M (III) X6 (M = Bi, Sb; X = halogen) double perovskites: A combined density functional theory and experimental study. *J. Am. Chem. Soc.* **139**(17), 6054–6057 (2017).
4. Bhamu, K. C., Soni, A. & Sahariya, J. Revealing optoelectronic and transport properties of potential perovskites Cs2PdX6 (X = Cl, Br): A probe from density functional theory (DFT). *Sol. Energy* **162**, 336–343 (2018).
5. Zhou, L., Xu, Y. F., Chen, B. X., Kuang, D. B. & Su, C. Y. Synthesis and photocatalytic application of stable lead-free Cs2AgBiBr 6 perovskite nanocrystals. *Small* **14**(11), 1703762 (2018).
6. Reshak, A. H. Ab initio study of TaON, an active photocatalyst under visible light irradiation. *Phys. Chem. Chem. Phys.* **16**(22), 10558–10565 (2014).
7. Arockiya Dass, K. T., Hossain, M. K. & Marasamy, L. Highly efficient emerging Ag2BaTiSe4 solar cells using a new class of alkaline earth metal-based chalcogenide buffers alternative to CdS. *Sci. Rep.* **14**(1), 1473 (2024).
8. Liang, Y. *et al.* Tapping the light emitting potential of chalcogenide perovskite SrHfS3 via Eu2+ doping. *Adv. Opt. Mater.* **12**(6), 2301977 (2024).
9. Tiwari, D., Hutter, O. S. & Longo, G. Chalcogenide perovskites for photovoltaics: Current status and prospects. *J. Phys. Energy* **3**(3), 034010 (2021).
10. Sopiha, K. V., Comparotto, C., Márquez, J. A. & Scragg, J. J. Chalcogenide perovskites: Tantalizing prospects, challenging materials. *Adv. Opt. Mater.* **10**(3), 2101704 (2022).
11. Hossain, M. K. *et al.* An extensive study on multiple ETL and HTL layers to design and simulation of high-performance lead-free CsSnCl3-based perovskite solar cells. *Sci. Rep.* **13**(1), 2521 (2023).
12. Yuan, M. *et al.* Controlling the band gap to improve open-circuit voltage in metal chalcogenide based perovskite solar cells. *Electrochim. Acta* **215**, 374–379 (2016).
13. Rani, U. *et al.* Electronic structure, theoretical power conversion efficiency, and thermoelectric properties of bismuth-based alkaline earth antiperovskites. *J. Mol. Model.* **29**(10), 329 (2023).
14. Leng, K., Xia, W. & Zhu, X. Advanced nanostructured perovskite oxides: Synthesis, physical properties, structural characterizations and functional applications. *Adv. Ceram. Energy Environ. Appl.* **1**, 13–81 (2021).
15. Ye, X. *et al.* Emergent physical properties of perovskite-type oxides prepared under high pressure. *Dalton Trans.* **51**(5), 1745–1753 (2022).
16. Pradhan, P. K., Mohanty, N. K., Mishra, G. K. & Behera, B. Concepts and recent advancements in perovskite metal oxides. In *Perovskite Metal Oxides* (eds Pradhan, P. K. *et al.*) 3–22 (Elsevier, 2023).
17. Rani, M. *et al.* Rare earth-based oxides double perovskites A2NiMnO6 (A= La and Gd): Applications in magneto-caloric, photocatalytic and thermoelectric devices. *Physica B* **680**, 415645 (2024).
18. Bairwa, J. K. *et al.* Modeling and simulation of multifaceted properties of X2NaIO6 (X = Ca and Sr) double perovskite oxides for advanced technological applications. *J. Mol. Model.* **29**(12), 379 (2023).
19. Rani, M. *et al.* Ab-initio calculations of structural, optoelectronic, thermoelectric, and thermodynamic properties of mixed-halide perovskites RbPbBr 3−xIx (x = 0 to 3): Applicable in renewable energy devices. *ECS J. Solid State Sci. Technol.* **12**(8), 083006 (2023).
20. Kumari, S. *et al.* Computational investigation of the fundamental physical properties of lead-free halide double perovskite Rb2NaCoX6 (X = Cl, Br, and I) materials: Potential prospects for sustainable energy. *Mod. Phys. Lett. B* **1**, 2450323 (2024).
21. Ravi, V. K. *et al.* Colloidal BaZrS3 chalcogenide perovskite nanocrystals for thin film device fabrication. *Nanoscale* **13**(3), 1616–1623 (2021).
22. Amrillah, T. *et al.* Environment-friendly copper-based chalcogenide thin film solar cells: Status and perspectives. *Mater. Horiz.* **10**(2), 313–339 (2023).
23. Altaf, A. *et al.* Metal/covalent organic framework encapsulated lead-free halide perovskite hybrid nanocatalysts: Multifunctional applications, design, recent trends, challenges, and prospects. *ACS Omega* **1**, 1 (2024).
24. Kumar, M. *et al.* Advances in green energy conversion efficiency and interfacial engineering investigations of lead-free FASnI3-based PSC device. *J. Phys. Chem. Solids* **193**, 112139 (2024).
25. Podapangi, S. K. *et al.* Green solvents, materials, and lead-free semiconductors for sustainable fabrication of perovskite solar cells. *RSC Adv.* **13**(27), 18165–18206 (2023).
26. Zhang, Y. *et al.* SCAPS simulation and DFT study of lead-free perovskite solar cells based on CsGeI3. *Mater. Chem. Phys.* **306**, 128084 (2023).
27. Dubey, A. *et al.* Lead-free alternative cation (Ethylammonium) in organometallic perovskites for thermoelectric applications. *J. Mol. Model.* **30**(3), 77 (2024).
28. Okumura, R., Oku, T. & Suzuki, A. Electronic structures and properties of lead-free cesium-or rubidium-based perovskite halide compounds by first-principles calculations. *Nano Trends* **4**, 100020 (2023).
29. Sarker, M. A., Muntasir, M., Momin, M. A., Solayman, M. & Islam, M. R. Pressure-induced structural, electronic, and optical properties of lead-free NaGeX3 (X = F, Cl, Br, and I) perovskites: First-principles calculation. *Adv. Theory Simulat.* **7**(7), 2400112 (2024).
30. Chauhan, A. & Oudhia, A. First-principle density functional theory-derived nonleaded KSn1−xGexI3-based perovskite solar cells: A theoretical study. *Energy Technol.* **12**(2), 2300772 (2024).
31. Ju, M. G., Dai, J., Ma, L. & Zeng, X. C. Perovskite chalcogenides with optimal bandgap and desired optical absorption for photovoltaic devices. *Adv. Energy Mater.* **7**(18), 1700216 (2017).
32. Tong, J. *et al.* Wide-bandgap metal halide perovskites for tandem solar cells. *ACS Energy Lett.* **6**(1), 232–248 (2020).
33. Swarnkar, A. *et al.* Are chalcogenide perovskites an emerging class of semiconductors for optoelectronic properties and solar cell? *Chem. Mater.* **31**(3), 565–575 (2019).
34. Basera, P. & Bhattacharya, S. Chalcogenide perovskites (ABS3; A = Ba, Ca, Sr; B= Hf, Sn): An emerging class of semiconductors for optoelectronics. *J. Phys. Chem. Lett.* **13**(28), 6439–6446 (2022).
35. Agiorgousis, M. L., Sun, Y. Y., Choe, D. H., West, D. & Zhang, S. Machine learning augmented discovery of chalcogenide double perovskites for photovoltaics. *Adv. Theory Simul.* **3**(1), 1900200 (2020).
36. Majhi, K. C. & Yadav, M. Transition metal-based chalcogenides as electrocatalysts for overall water splitting. *ACS Eng. Au* **3**(5), 278–284 (2023).
37. Cen, Y. L. *et al.* Design of lead-free and stable two-dimensional Dion–Jacobson-type chalcogenide perovskite A′ La2B3S10 (A′ = Ba/Sr/Ca; B= Hf/Zr) with optimal band gap, strong optical absorption, and high efficiency for photovoltaics. *Chem. Mater.* **32**(6), 2450–2460 (2020).
38. Mustafa, G. M. *et al.* First-principles calculations to investigate HgY2S/Se4 spinel chalcogenides for optoelectronic and thermoelectric applications. *J. Market. Res.* **22**, 97–106 (2023).
39. Perera, S. *et al.* Chalcogenide perovskites—An emerging class of ionic semiconductors. *Nano Energy* **22**, 129–135 (2016).

40. Shaili, H. *et al.* Synthesis of the Sn-based CaSnS3 chalcogenide perovskite thin film as a highly stable photoabsorber for optoelectronic applications. *J. Alloys Compd.* **851**, 156790 (2021).
41. Pandit, N. *et al.* Physical properties and power conversion efficiency of SrZrX3 (X = S and Se) chalcogenide perovskite solar cell. *Mod. Phys. Lett. B* **1**, 2450345 (2024).
42. Pandit, N. *et al.* Effect of anion ($S^{-2}$ & $Se^{-2}$) replacement on photovoltaic properties in transition metal (Ba-Barium) chalcogenide perovskites. *Int. J. Mod. Phys. B* **1**, 2550059 (2024).
43. Nishigaki, Y. *et al.* Extraordinary strong band-edge absorption in distorted chalcogenide perovskites. *Solar Rrl* **4**(5), 1900555 (2020).
44. Majhi, K. C. & Yadav, M. Bimetallic chalcogenide nanocrystallites as efficient electrocatalyst for overall water splitting. *J. Alloys Compds.* **852**, 156736 (2021).
45. Sun, Y. Y., Agiorgousis, M. L., Zhang, P. & Zhang, S. Chalcogenide perovskites for photovoltaics. *Nano Lett.* **15**(1), 581–585 (2015).
46. Du, J. & Shi, J. J. 2D Ca3Sn2S7 chalcogenide perovskite: A graphene-like semiconductor with direct bandgap 0.5 eV and ultrahigh carrier mobility $6.7 \times 104$ $cm^2$ $V^{-1}$ $s^{-1}$. *Adv. Mater.* **31**(51), 1905643 (2019).
47. Du, J. *et al.* Cerium-based lead-free chalcogenide perovskites for photovoltaics. *Phys. Rev. B* **104**(23), 235206 (2021).
48. Thakur, N., Kumar, P., Neffati, R. & Sharma, P. Design and simulation of chalcogenide perovskite BaZr (S, Se) 3 compositions for photovoltaic applications. *Phys. Scr.* **98**(6), 065921 (2023).
49. Liu, D., Peng, H., He, J. & Sa, R. Alloy engineering to tune the optoelectronic properties and photovoltaic performance for Hf-based chalcogenide perovskites. *Mater. Sci. Semicond. Process.* **169**, 107919 (2024).
50. Liu, D., Zeng, H., Peng, H. & Sa, R. Computational study of the fundamental properties of Zr-based chalcogenide perovskites for optoelectronics. *Phys. Chem. Chem. Phys.* **25**(19), 13755–13765 (2023).
51. Zhang, H. *et al.* Prediction and synthesis of a selenide perovskite for optoelectronics. *Chem. Mater.* **35**(11), 4128–4135 (2023).
52. Peng, Y., Sun, Q., Chen, H. & Yin, W. J. Disparity of the nature of the band gap between halide and chalcogenide single perovskites for solar cell absorbers. *J. Phys. Chem. Lett.* **10**(16), 4566–4570 (2019).
53. Heyd, J., Scuseria, G. E. & Ernzerhof, M. Hybrid functionals based on a screened Coulomb potential. *J. Chem. Phys.* **118**(18), 8207–8215 (2003).
54. Shakil, M. *et al.* Theoretical investigation of structural and mechanical stability, electronic, optical, and transport behaviour of double halide perovskites K2GaBiX6 (X = Cl, Br, and I) for optoelectronic applications. *Comput. Condens. Matter* **1**, e00941 (2024).
55. Cheng, J. *et al.* From VIB-to VB-Group transition metal disulfides: Structure engineering modulation for superior electromagnetic wave absorption. *Nano-Micro Lett.* **16**(1), 29 (2024).
56. *The Materials Project*. https://materialsproject.org/.
57. Shirley, E. L., Allan, D. C., Martin, R. M. & Joannopoulos, J. D. Extended norm-conserving pseudopotentials. *Phys. Rev. B* **40**(6), 3652 (1989).
58. Smrčok, Ľ, Mach, P. & Le, A. Bail b. Department of Theoretical Chemistry, Institute of Inorganic Chemistry, Slovak Academy of Sciences, Dúbravská cesta 9, SK-845 36. *J. Appl. Crystallogr.* **14**, 357–361 (1981).
59. Ur Rehman, S. *et al.* Pressure induced structural and optical properties of cubic phase SnSe: An investigation for the infrared/mid-infrared optoelectronic devices. *J. Alloys Compds.* **695**, 194–201 (2017).
60. Wooten, F. *Optical Properties of Solids* (Academic Press, 1972).
61. Segall, M. D. *et al.* First-principles simulation: Ideas, illustrations and the CASTEP code. *J. Phys. Condens. Matter* **14**(11), 2717 (2002).
62. Jana, D., Sun, C. L., Chen, L. C. & Chen, K. H. Effect of chemical doping of boron and nitrogen on the electronic, optical, and electrochemical properties of carbon nanotubes. *Prog. Mater. Sci.* **58**(5), 565–635 (2013).
63. Saha, S., Sinha, T. P. & Mookerjee, A. Electronic structure, chemical bonding, and optical properties of paraelectric BaTiO3. *Phys. Rev. B* **62**(13), 8828 (2000).
64. Yang, M. *et al.* Comparison of optical properties between Wurtzite and zinc-blende Ga0.75Al0.25N. *Optik* **125**(1), 424–427 (2014).
65. Saliba, M. *et al.* Incorporation of rubidium cations into perovskite solar cells improves photovoltaic performance. *Science* **354**(6309), 206–209 (2016).
66. Saliba, M. *et al.* Cesium-containing triple cation perovskite solar cells: Improved stability, reproducibility and high efficiency. *Energy Environ. Sci.* **9**(6), 1989–1997 (2016).
67. Gautam, S. & Gupta, D. C. Exploring the structural, mechanical, magneto-electronic and thermophysical properties of f electron based XNpO3 perovskites (X = Na, Cs, Ca, Ra). *Sci. Rep.* **14**(1), 8918 (2024).
68. Randall, C. A., Bhalla, A. S., Shrout, T. R. & Cross, L. E. Classification and consequences of complex lead perovskite ferroelectrics with regard to B-site cation order. *J. Mater. Res.* **5**(4), 829–834 (1990).
69. Han, G. *et al.* Additive selection strategy for high performance perovskite photovoltaics. *J. Phys. Chem. C* **122**(25), 13884–13893 (2018).
70. Aleksandrov, K. S. The sequences of structural phase transitions in perovskites. *Ferroelectrics* **14**(1), 801–805 (1976).
71. Shannon, R. D. Revised effective ionic radii and systematic studies of interatomic distances in halides and chalcogenides. *Acta Crystallogr. Sect. A Cryst. Phys. Diffract. Theor. Gen. Crystallogr.* **32**(5), 751–767 (1976).
72. Xu, N. *et al.* First-principles investigations for the hydrogen storage properties of XVH3 (X¼Na, K, Rb, Cs) perovskite type hydrides. *J. Mater. Res. Technol.* **2**(6), 4825 (2023).
73. Li, Z. *et al.* Scalable fabrication of perovskite solar cells. *Nat. Rev. Mater.* **3**(4), 1–20 (2018).
74. Aranda, C. *et al.* Formation criteria of high efficiency perovskite solar cells under ambient conditions. *Sustain. Energy Fuels* **1**(3), 540–547 (2017).
75. Lu, Y. *et al.* Theoretical prediction on the stability, elastic, electronic and optical properties of MAB-phase M4 AlB4 compounds (M= Cr, Mo, W). *RSC Adv.* **14**(2), 1186–1194 (2024).
76. Ono, S. & Kobayashi, D. Role of the M point phonons for the dynamical stability of B2 compounds. *Sci. Rep.* **12**(1), 7258 (2022).
77. Allal, A., Halit, M., Saib, S., Luo, W. & Ahuja, R. Phase stability, phonon, electronic, and optical properties of not-yet-synthesized CsScS2, CsYS2, and APmS2 (A = Li, Na, K, Rb, Cs) materials: Insights from first-principles calculations. *Mater. Sci. Semicond. Process.* **150**, 106936 (2022).
78. Sun, Q., Chen, H. & Yin, W. J. Do chalcogenide double perovskites work as solar cell absorbers: a first-principles study. *Chem. Mater.* **31**(1), 244–250 (2018).
79. Quarti, C. *et al.* Structural and optical properties of methylammonium lead iodide across the tetragonal to cubic phase transition: Implications for perovskite solar cells. *Energy Environ. Sci.* **9**(1), 155–163 (2016).
80. Challinger, S. E., Baikie, I. D., Harwell, J. R., Turnbull, G. A. & Samuel, I. D. An investigation of the energy levels within a common perovskite solar cell device and a comparison of DC/AC surface photovoltage spectroscopy Kelvin probe measurements of different MAPBI3 perovskite solar cell device structures. *MRS Adv.* **2**(21–22), 1195–1201 (2017).
81. Li, X. L. *et al.* (C6 H5 NH3) BiI4: A lead-free perovskite with > 330 days humidity stability for optoelectronic applications. *J. Mater. Chem. A* **7**(26), 15722–15730 (2019).
82. Chen, L. *et al.* Lead-free perovskite narrow-bandgap oxide semiconductors of rare-earth manganates. *ACS Omega* **5**(15), 8766–8776 (2020).

83. Sujith, C. P., Joseph, S., Mathew, T. & Mathew, V. First-principles investigation of structural, electronic and optical properties of quasi-one-dimensional barium cadmium chalcogenides Ba2CdX3 (X = S, Se, Te) using HSE06 and GGA-PBE functionals. *J. Phys. Chem. Solids* **161**, 110488 (2022).
84. Tang, T. & Tang, Y. Promising anti-perovskites Ba6CCh4 (Ch = S, Se, Te) with direct bandgaps and great light absorption: A first-principles study. *Inorg. Chem. Commun.* **157**, 111337 (2023).
85. Sze, S. M. & Ng, K. K. *Physics of Semiconductor Devices* 3rd edn. (Wiley, 2007).
86. Adachi, S. *Properties of Semiconductor Alloys: Group-IV, III-V and II-VI Semiconductors* (Wiley, 2005).
87. Umari, P., Mosconi, E. & De Angelis, F. Relativistic GW calculations on CH3NH3PbI3 and CH3NH3SnI3 perovskites for solar cell applications. *Sci. Rep.* **4**(1), 4467 (2014).
88. Edwards, D. F. & Ochoa, E. Infrared refractive index of silicon. *Appl. Opt.* **19**(24), 4130–4131 (1980).
89. Davis, P. W. & Shilliday, T. S. Some optical properties of cadmium telluride. *Phys. Rev.* **118**(4), 1020 (1960).
90. Shukla, A., Sharma, V. K., Gupta, S. K. & Verma, A. S. Investigations of fundamental physical and thermoelectric properties of methylammonium lead iodide (CH3NH3PbI3) perovskites. *Mater. Res. Express* **6**(12), 126323 (2020).
91. Katagiri, H., Ishigaki, N., Ishida, T. & Saito, K. Characterization of Cu2ZnSnS4 thin films prepared by vapor phase sulfurization. *Jpn. J. Appl. Phys.* **40**(2R), 500 (2001).
92. Cardona, M. Optical properties and band structure of SrTiO3 and BaTiO3. *Phys. Rev.* **140**(2A), A651 (1965).
93. Kojima, A., Teshima, K., Shirai, Y. & Miyasaka, T. Organometal halide perovskites as visible-light sensitizers for photovoltaic cells. *J. Am. Chem. Soc.* **131**(17), 6050–6051 (2009).


## Author contributions

E.Kh.M.: Methodology, Data curation, Formal analysis, Investigation, Software, Visualization, Writing-original draft. M.T.: Conceptualization, Investigation, Methodology, Software, Supervision, Visualization, Writing—original draft, Writing—review & editing. S. I. E.: Methodology, Writing—review & editing, Supervision. A.A.F.: Supervision. All authors reviewed the manuscript.

## Funding

Open access funding provided by The Science, Technology & Innovation Funding Authority (STDF) in cooperation with The Egyptian Knowledge Bank (EKB).

## Competing interests

The authors declare no competing interests.

## Additional information

**Correspondence** and requests for materials should be addressed to M.T.

**Reprints and permissions information** is available at www.nature.com/reprints.

**Publisher's note** Springer Nature remains neutral with regard to jurisdictional claims in published maps and institutional affiliations.